Supplementary Information

1. Determining absorption and reflection of GaAs nanowire-arrays

In a center-mount mode for absorption measurements of non-opaque samples (e.g. GaAs nanowire-arrays embedded in peeled-off PDMS), each sample was supported on a quartz slide and placed at the center of the sphere. The rotational stage to which the sample was mounted permitted eucentric rotation in one azimuthal direction with 0.1^{o} resolution. Tilting angles of $0 - 60^{o}$ were used for the center-mount absorption measurements of the sample. The 0% absorption standard was assigned using a bare quartz slide that was mounted at the same location as the sample. For the center-mount measurements, each absorption spectrum was determined by the wavelength-dependent signal normalized to a 0% absorption standard obtained using a bare quartz slide. This procedure was performed at each incident angle, to obtain the angle-resolved absorption spectra.

In a rear-mount mode for reflection measurements of opaque samples (e.g. as-grown GaAs NW arrays on GaAs or Si substrates; or NW arrays embedded in PDMS placed on a Ag back reflector), each sample was mounted behind a 2 mm-diameter port aperture at the rear port of the sphere with normal incidence of light. The wire-array reflection was normalized to a reflectance standard (99%, LabSphere, Inc) that was placed on the same location behind the port aperture at the rear port of the sphere. For the reflection measurements of as-grown GaAs NW arrays on crystalline substrates, the sample was placed directly against the port aperture so that the small-spot beam illuminated only the NW arrays. For the measurements of NW arrays on a specular back-reflector, the NW array that had been embedded in a PDMS film was placed on a quartz slide that had been coated with 500 nm of evaporated Ag. Before deposition of the Ag film, a 2 nm Ge seed layer was evaporated to produce <10 nm rms roughness in surface morphology.[1] For opaque samples, including nanowire-arrays on crystalline substrates or those placed on a specular back-reflector, the absorption was

determined from reflection measurements only: $A(\lambda,\theta) = 1 - R(\lambda,\theta)$. The reflection spectrum was calculated from the wavelength-dependent signals normalized by the signals that were measured from the reflection standard.

Figure S1 displays the angle-dependent reflection measurements of these wire-arrays, which exhibited a broadband reflection of < 10%. The antireflective properties of off-normal-incident absorption were slightly weaker than those measured at normal incidence.

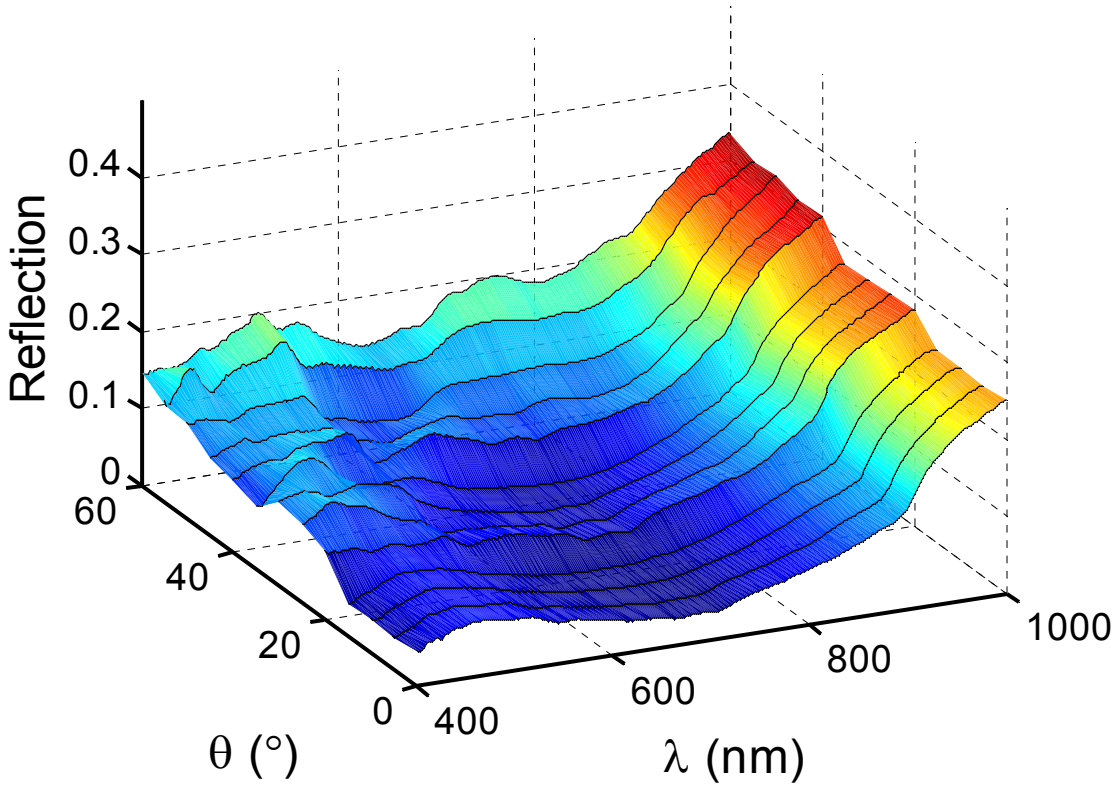

Figure S1. Angle-dependent optical reflection of GaAs NW arrays.

2. Open-circuit potential at optimal doping

The results reported in the main text were obtained using wire arrays that had a donor concentration which maximized the open-circuit potential of the photoanode (Figure S2). The doping concentration of the wires was controlled by varying the Si_2H_6 flow rate during MOCVD growth, from 0.004 – 0.5 sccm. A Si_2H_6 flow rate of 0.05 sccm was found to be

optimal, and was used for all the n-GaAs NW photoelectrodes discussed in this paper.

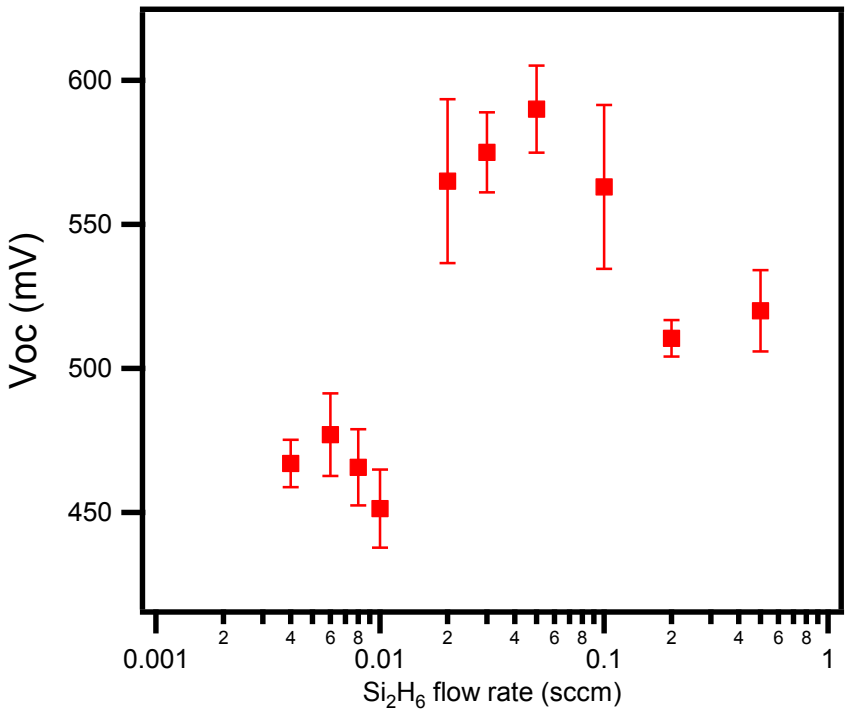

Figure S2. Open-circuit voltage of n-GaAs NW/CH_3CN-$FeCp_2^{+/0}$ junctions as a function of flow rates of disilane (Si_2H_6, 0.004 − 0.5 sccm) during MOCVD growth. All of the open-circuit voltages were measured under W-halogen illumination at 1-Sun (100 mW cm^{-2}) equivalent of light intensity.

3. Photoelectrochemical current density–potential (*J–E*) measurements

The *J-E* data were reported both as-collected and after correction for concentration overpotential and solution resistance losses in the electrolyte.[2] A Pt disk electrode (area: 0.031416 cm^2) was used to measure the uncompensated ohmic resistance of the cell as well as the anodic and cathodic limiting current densities, to allow for robust correction of the concentration over-potentials. Figure S3 shows the polarization data of the Pt disk electrode before and after correction for concentration overpotential and solution resistance losses, using the correction protocol described previously.[3,4] The values of the cathodic and anodic limiting current densities, respectively, were estimated from the saturation currents of a

specific photoelectrode of interest in the cathodic mass-transport-limiting condition, and from the limiting current density of a similarly sized Pt disk electrode under its anodic mass-transport-limiting condition in the same cell configuration. Typical values were -0.16 $mA \cdot cm^{-2}$ for the cathodic current density and 94.7 $mA \cdot cm^{-2}$ for the anodic limiting current density. The uncompensated ohmic resistances, typically ~290 Ω, were extracted from the inverse slope of the linear region of the polarization curves for the Pt disk electrode.

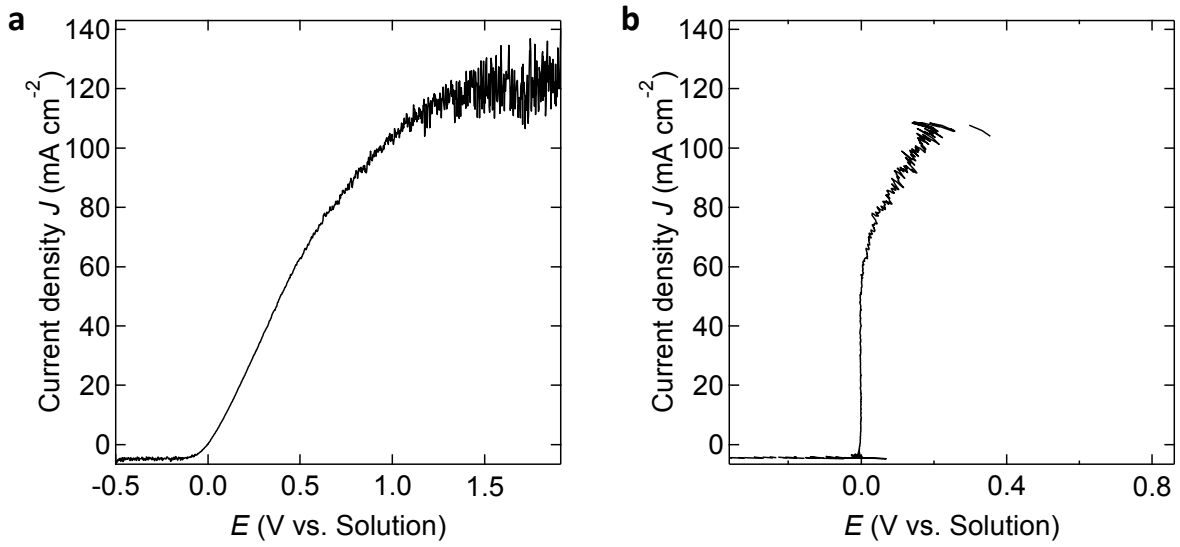

Figure S3. Typical polarization data for a Pt disk electrode (electrode area: 0.031416 cm^2) (a) before and (b) after correction for concentration overpotential and solution resistance losses.

4. Photoelectrochemical external quantum yields measurements

External quantum yields measurements were performed after the *J-E* measurements in the photoelectrochemical cell that contained the same CH_3CN–1.0 M $LiClO_4$–0.5 mM $FeCp_2^+$–90 mM $FeCp_2^0$ electrolyte. The light from a 150 W xenon arc lamp was chopped at 30 Hz, and then passed through a quarter-wave monochromator (Oriel MS257). The exit beam was passed through a long-pass filter to remove higher-order diffractions, and was then split off by a quartz slide and directed to a reference Si photodiode that allowed for correction for any

fluctuations in the intensity of the light source. The main beam was directed onto the photoelectrode in the photoelectrochemical cell. The light intensity at the photoelectrode was determined using a calibrated Si photodiode that was placed at the same position as the photoelectrode. A Pyrex glass slide was placed in front of the calibrated Si photodiode. This procedure corrected for the absorption and reflection loss of the optical window at the bottom of the cell. A Gamry G300 potentiostat was used to measure the photocurrent at short circuit. The signals from both the potentiostat output and from the calibrated Si photodiode were collected by individual lock-in amplifiers (Stanford Research System 830), and the data were acquired and digitized by a computer that was controlled by a custom LabVIEW program. Photocurrent densities during acquisition the spectral response data were on the order of 10 $nA \cdot cm^{-2}$. The wavelength-dependent spectral response data from a Si photodiode that was placed at the same position as the photoelectrodes were obtained both inside the electrochemical cell and without the cell (Figure S3). A strong optical absorption at ~ 450 nm was observed due to dissolved $FeCp_2^+$ species. The ratio of the measured responses was used to correct for any optical absorption or transmission losses in the cell.

5. Mott-Schottky analysis

The built-in voltages, V_{bi}, of GaAs nanowire-array /CH_3CN-$FeCp_2^{+/0}$, planar GaAs (100) /CH_3CN-$FeCp_2^{+/0}$, and planar GaAs (110) planar /CH_3CN-$FeCp_2^{+/0}$ junctions were determined from electrochemical impedance data. The impedance data were acquired with a Gamry Reference 600 analyzer with an electrochemical interface, and the data were analyzed using custom software. The liquid solution consisted of 0.5 mM ferrocenium, 90 mM ferrocene, and 1M $LiClO_4$ as the supporting electrolyte. All electrodes were etched immediately before each experiment. A 15 mV (RMS) AC signal with a frequency ranging from 1 Hz to 1 MHz was superimposed on a DC bias from 0 to 0.4 V vs. the solution potential. The method used for extraction of built-in voltages by fitting frequency-dependent impedance data has been described previously. [5]

The differential capacitance of the GaAs space-charge region was computed by fitting with the aforementioned model using the equation: [2]

$$2\pi f C_{sc} = \frac{1+\sqrt{1-4(Z_{im}/R_{sc})^2}}{2Z_{im}} \quad (1)$$

where f is the frequency of the ac signal and Z_{im} is the imaginary part of the measured impedance, Z, at a certain dc bias. R_{SC} values were equivalent to the diameter of a semicircular fit to the Z_{im} vs. Z real plot (Nyquest plot, where Z real is the real part of the measured impedance Z). For planar GaAs/$FeCp_2^{+/0}$ interfaces, the capacitance of GaAs the space-charge region was then related to the built-in voltage by the Mott-Schottky equation:

$$C^{-2} = \frac{2}{q\,\epsilon\epsilon_0 N_d A_s^{\,2}}\left(E + V_{bi} - \frac{kT}{q}\right) \quad (2)$$

where ε is the dielectric constant of GaAs, ε_0 is the electrical permittivity of vacuum, and A_s is the total area of the semiconductor/liquid junction, which equals the product of the projected area of an electrode and roughness factor, γ, of the electrode. The built-in voltage can be determined by extrapolation of the E vs. C^{-2} plot to infinite capacitance, followed by application of the correction term kT/q. Electrodes that yielded non-linear plots (least square fit R^2<0.99) for the frequency values examined were considered defective. Figure S5 compares the Mott-Schottky plots of planar GaAs (110)/CH_3CN-$FeCp_2^{+/0}$ and planar GaAs (100) /CH_3CN-$FeCp_2^{+/0}$ junctions. The measured built-in voltage was 1.23±0.04V for GaAs (110) vs. 1.22±0.04V for GaAs (100). The slope of the E vs. C^{-2} plot gave a value for the dopant density of $3.11-3.32\times10^{17}$ for GaAs (110) and $1.03-1.07\times10^{17}$ for GaAs (100), in good agreement with the values specified by the manufacturer.

For GaAs NW/$FeCp_2^{+/0}$ interfaces, the capacitance of the NW space-charge regions was calculated numerically and then compared to the experimentally measured capacitance, to determine the doping concentration of n-GaAs NWs. For simplicity of calculation, the

geometry of each NW was assumed to be 3 μm long and to have a cylindrical diameter of 150 nm, which corresponds to the dimensions of the NWs in the experiment. Abrupt depletion was also assumed, meaning that the fully depleted region in the shell ($a<r<b$) of a NW had an abrupt and distinctive boundary with the remaining portion of the NW. A schematic drawing for the space-charge distribution in a cylindrical NW is illustrated in Fig. S6a. By solving Possion's equation in the shell region, the inner radius for the neutral region, a, can be determined by the doping concentration of the NW and the bias applied to the NW/liquid interface. The differential capacitances, C, of the NW depletion regions contain contributions from the NW sidewalls as well as from the top surfaces of the NW. The value of C^{-2} was then plotted as a function of the applied bias, E, at various doping concentrations. The doping concentration of n-GaAs NWs was then determined by comparing the data with a series of C^{-2} vs. E curves, as shown in Fig. S6b.

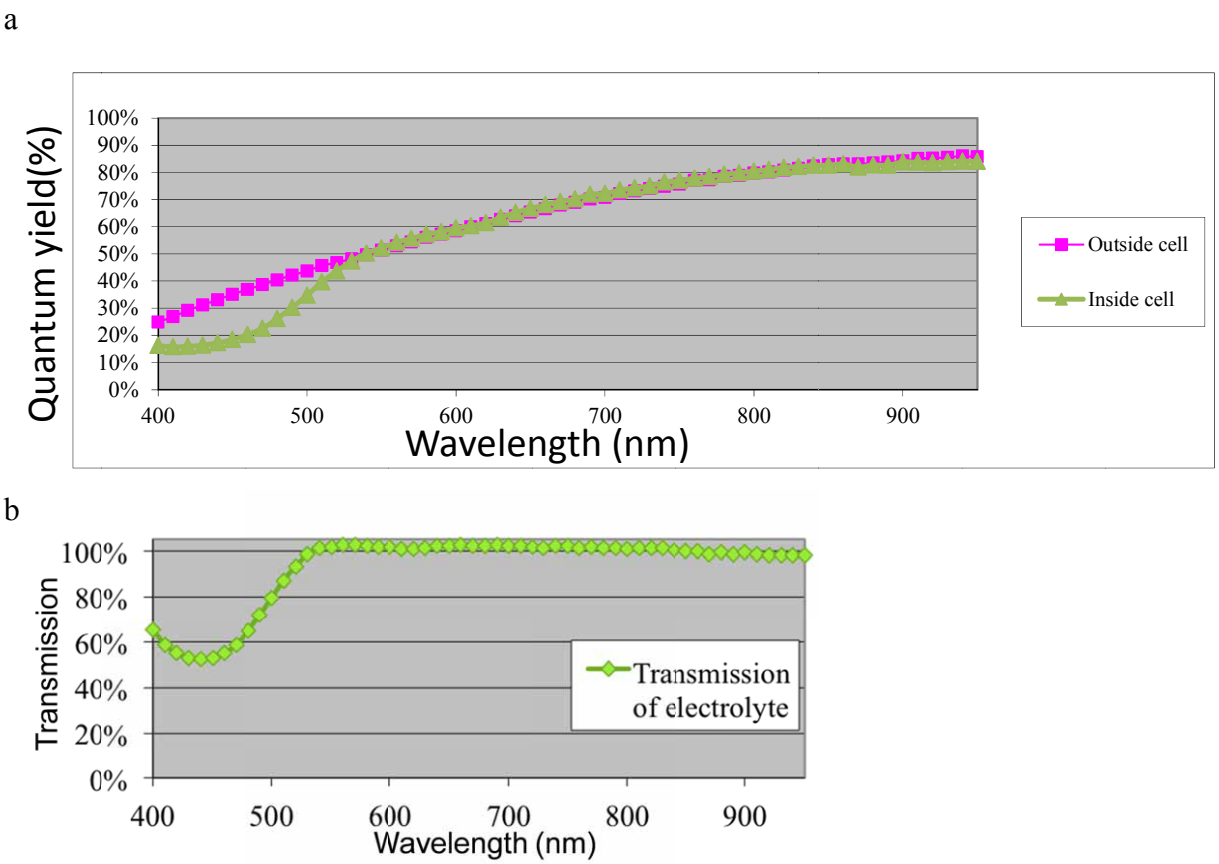

Figure S4. (a) Wavelength-dependent spectral response data for a Si photodiode, measured both inside the electrochemical cell and without the cell. (b) Solution absorptivity data calculated from the quantum yield measurements in (a).

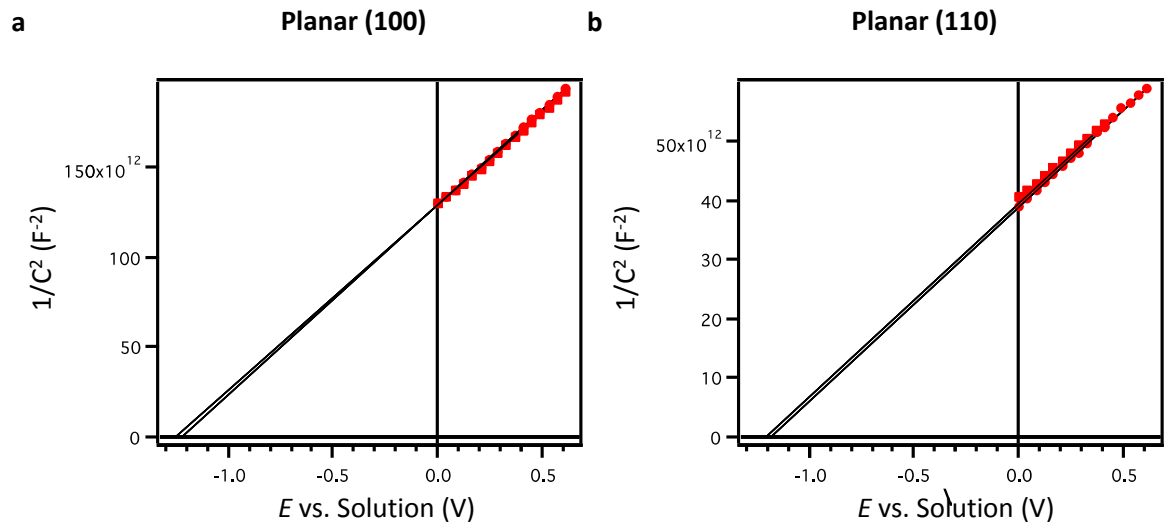

Figure S5. Mott-Schottky plots of (a) planar GaAs (100)/ CH_3CN-$FeCp_2^{+/0}$ and (b) planar GaAs (110)/ CH_3CN-$FeCp_2^{+/0}$ junctions. The experimental conditions were identical to those

used for the measurements shown in Fig. 4. The electrode areas were ~0.2 cm^{-2} and ~0.3 cm^{-2} for the planar (100) and (110) photoelectrodes, respectively. The data shown represent upper bound and lower bound values for the measured built-in voltages.

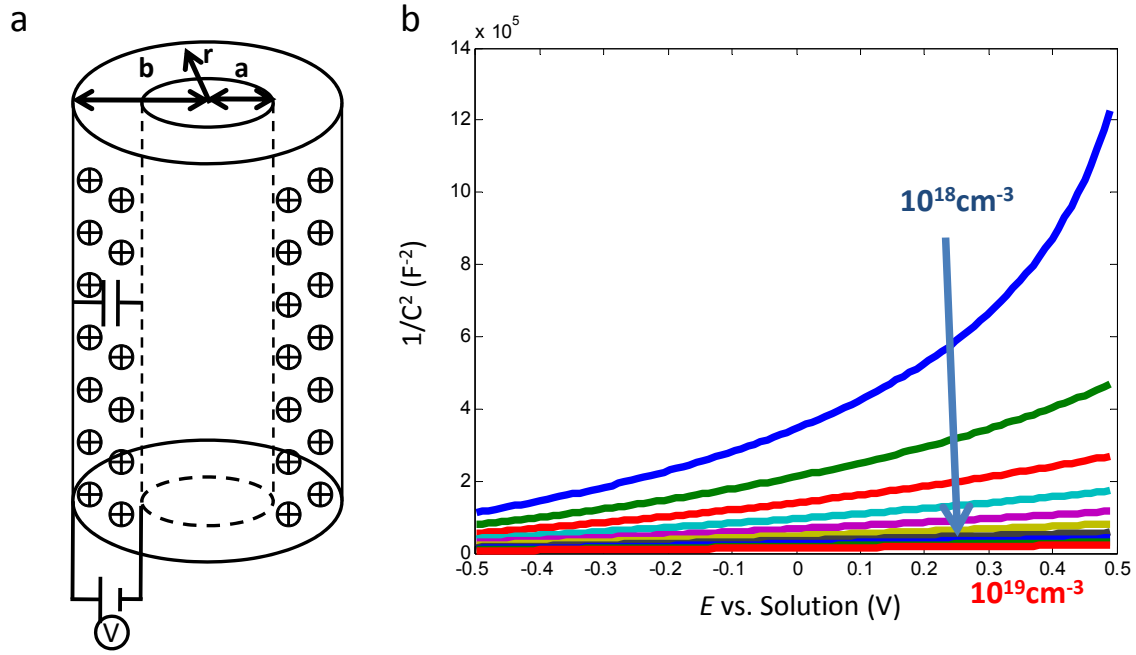

Figure S6. (a) Schematic drawing of the NW sidewall capacitance in the depletion region. The depletion region has an abrupt margin. A bias is applied across the junction, and *b* and *a* are the outer and inner radii, respectively, that define the depletion region. (b) C^{-2} vs. E data for a single nanowire as a function of the doping concentration, over the range from 10^{18} cm^{-3} to 10^{19} cm^{-3}. The nanowire was assumed to be 3 μm long and 135 nm in diameter.

6. Simulated absorption spectra dependent on wire radius

Absorption spectra at normal incidence were simulated for varying wire radii, while holding the wire length and wire pitch constant. The resonant wavelengths were red-shifted with increasing wire radii. This result is consistent with the hypothesis that excitation of resonant optical waveguide modes is responsible for the enhanced absorption because the resonant wavelengths for optical waveguide modes are proportional to the radius of the waveguide.

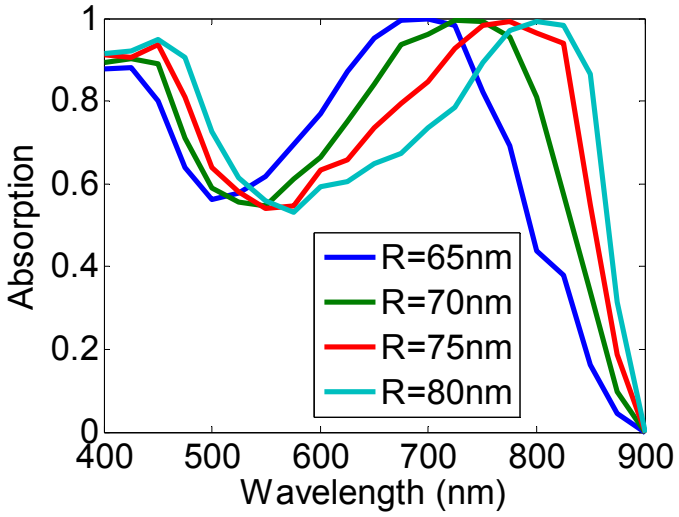

Figure S7. Simulated absorption spectra for various wire radii.

7. Power absorption profiles of nanowire cross sections

These power absorption mode profiles of nanowire cross sections shown in Figure S8 are analogs to the electric field intensity profiles shown in (Figure 2e) in the main text. Calculating the power absorbed from the electric field intensity only yields non-zero values field components within the material (k>0), emphasizing clearly the characteristic mode profile observed within the wire. This mode profile is especially useful at short wavelengths (i.e. 440 nm), for which the large absorption coefficient of GaAs causes the mode to decay quickly and to have a relatively small amplitude within the wire relative to the electric field intensity in free space. Hence such modes are difficult to identify from solely the profile of the electric field intensity. The fine, pixilated rims around some of the wire absorption profiles are artifacts of the simulation.

8. Field intensity profiles for single wires

Mode profiles at 440 nm and 710 nm at normal incidence are shown below for an isolated NW and for a NW in a periodic array. Both electric field intensity profiles for the isolated NW were qualitatively identical, although quantitatively they were less intense than those computed for the NW in an array. These findings support the conclusion that the NWs are

acting as isolated optical waveguides, and that coupling into the waveguide modes is enhanced by scattering events in the NW-array.

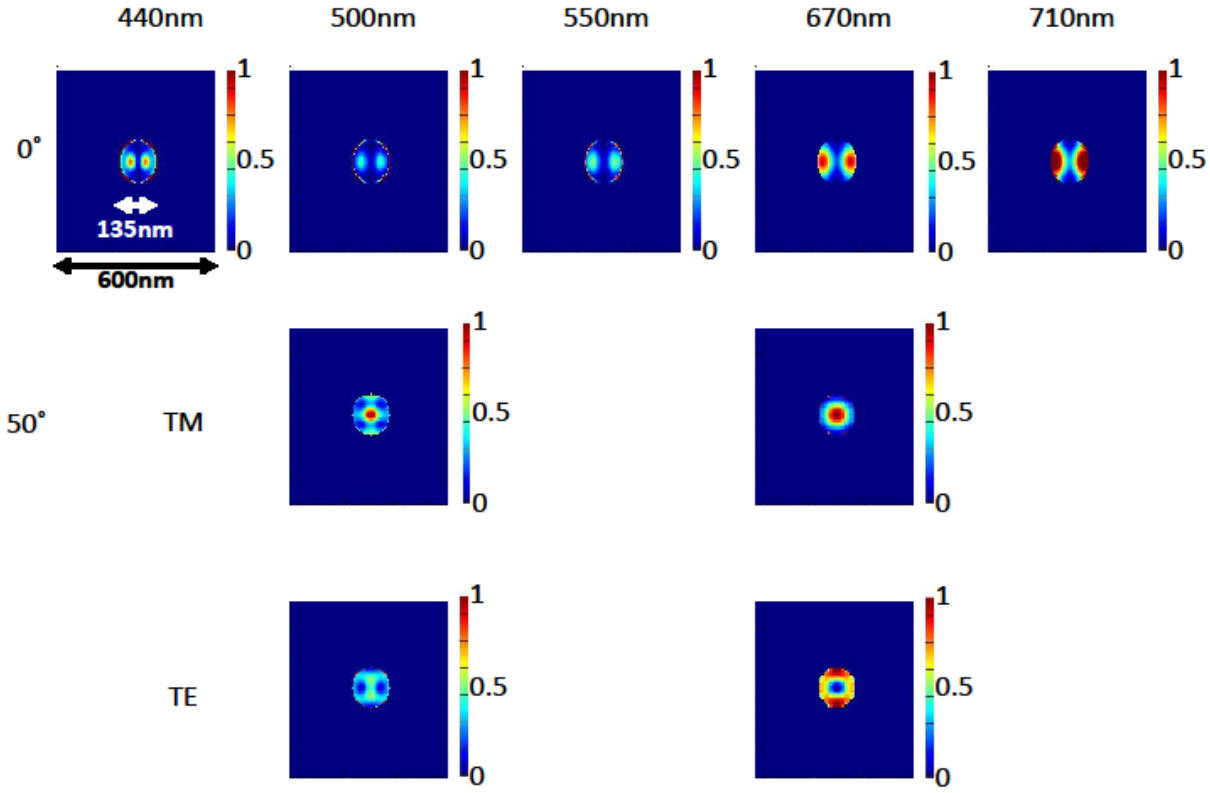

Figure S8. Simulated power absorption profiles of wire cross sections at various wavelengths, incident angles and polarizations, as calculated by 3D-FDTD methods. The data illustrate the optical waveguide mode profiles within the nanowire (the field of view is one periodic unit of the NW-array).

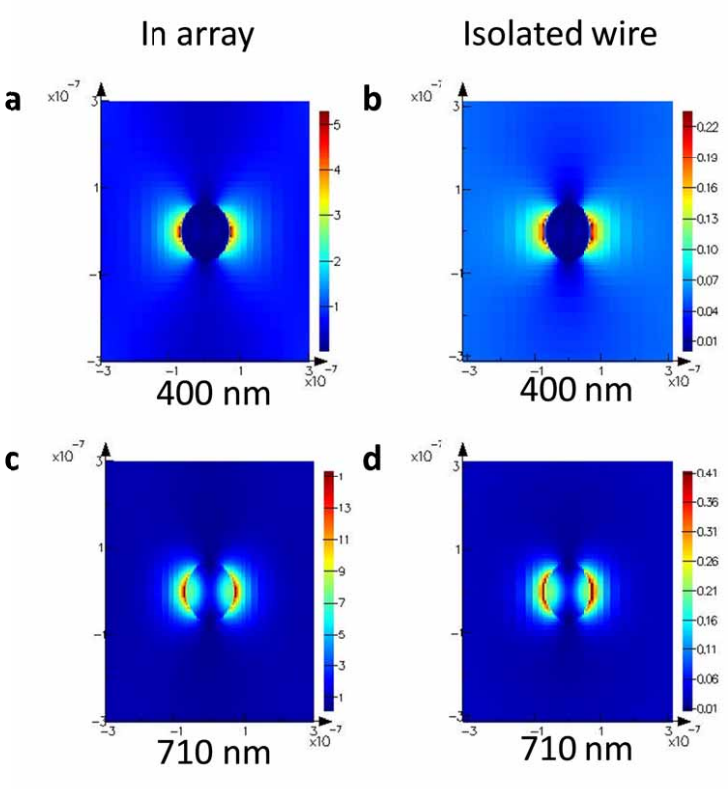

Figure S9. Intensity profiles of electric field at 400 and 710 nm for an isolated wire ((b) and (d)) vs. a wire in a periodic array ((a) and (c)).

9. Absorption at 50˚ off-normal incidence

Figure S10 overlays the absorption vs. wavelength for the GaAs NW-arrays at 50˚ incidence, for both TM and TE polarization, and their average, with the normal incidence absorption. The resonant wavelengths clearly changed between normal and off-normal incidence, for both polarizations, as discussed in the main text.

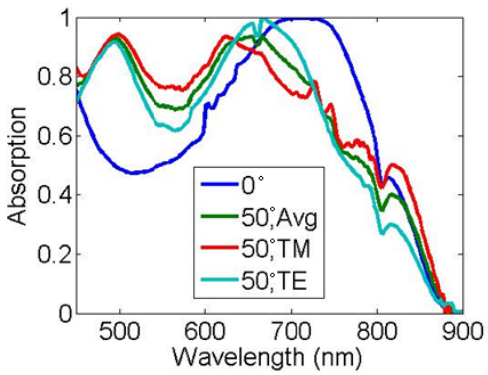

Figure S10. Simulated absorption spectra of the GaAs NW-arrays at 50˚ incidence for both TM and TE polarization and their average, compared to the absorption at 0˚ incidence.

10. Electric and magnetic field equations and the eigenvalue equations

Optical waveguide modes are solutions to Maxwell's equations, which simplify to the following equation for a sourceless material:

$$\nabla \times \vec{E} = -i\omega\mu\vec{H}$$

$$\nabla \times \vec{H} = i\omega\epsilon\vec{E}$$

The solution to these equations inside the wire and in radial coordinates leads to:

$$E_z(r,\theta,z) = A_{mn}J_m(k_1 r)e^{i(\omega t - m\theta - \beta z)}$$

$$E_r(r,\theta,z) = [-A_{mn}\frac{i\beta}{k_1}J'_m(k_1 r) - B_{mn}\frac{\omega\mu_1 m}{k_1^2 r}J_m(k_1 r)]e^{i(\omega t - m\theta - \beta z)}$$

$$E_\theta(r,\theta,z) = [-A_{mn}\frac{m\beta}{k_1^2 r}J_m(k_1 r) + B_{mn}\frac{i\omega\mu_1}{k_1}J'_m(k_1 r)]e^{i(\omega t - m\theta - \beta z)}$$

$$H_z(r,\theta,z) = B_{mn}J_m(k_1 r)e^{i(\omega t - m\theta - \beta z)}$$

$$H_r(r,\theta,z) = \left[-B_{mn}\frac{i\beta}{k_1}J'_m(k_1 r) - A_{mn}\frac{\omega\epsilon_1 m}{k_1^2 r}J_m(k_1 r)\right]e^{i(\omega t - m\theta - \beta z)}$$

$$H_\theta(r,\theta,z) = [-B_{mn}\frac{m\beta}{k_1^2 r}J_m(k_1 r) - A_{mn}\frac{i\omega\epsilon_1}{k_1}J'_m(k_1 r)]e^{i(\omega t - m\theta - \beta z)}$$

The solution to these equations outside the wire for guided modes leads to:

$$E_z(r,\theta,z) = C_{mn}K_m(k_2 r)e^{i(\omega t - m\theta - \beta z)}$$

$$E_r(r,\theta,z) = [C_{mn}\frac{i\beta}{k_2}K'_m(k_2 r) + D_{mn}\frac{\omega\mu_2 m}{k_2^2 r}K_m(k_2 r)]e^{i(\omega t - m\theta - \beta z)}$$

$$E_\theta(r,\theta,z) = [C_{mn}\frac{m\beta}{k_2^2 r}K_m(k_2 r) - D_{mn}\frac{i\omega\mu_2}{k_2}K'_m(k_2 r)]e^{i(\omega t - m\theta - \beta z)}$$

$$H_z(r,\theta,z) = D_{mn}K_m(k_2 r)e^{i(\omega t - m\theta - \beta z)}$$

$$H_r(r,\theta,z) = \left[D_{mn}\frac{i\beta}{k_2}K'_m(k_2 r) - C_{mn}\frac{\omega\epsilon_2 m}{k_2^2 r}K_m(k_2 r)\right]e^{i(\omega t - m\theta - \beta z)}$$

$$H_\theta(r,\theta,z) = [D_{mn}\frac{m\beta}{k_2^2 r}K_m(k_2 r) + C_{mn}\frac{i\omega\epsilon_2}{k_2}K'_m(k_2 r)]e^{i(\omega t - m\theta - \beta z)}$$

Notation is consistent with that found in the main text, with the addition of coefficients A_{mn}, B_{mn}, C_{mn}, and D_{mn} which depend on the mode. The solution outside the wire for leaky modes simply requires replacing the K_{mn} terms in the equations above with $-H_{mn}$. To determine the coefficients and obtain the eigenvalue equation, the boundary conditions of continuity of the z and θ components of the electric and magnetic fields at the wire/air interface must be applied.

11. Electric field intensity mode profiles

By taking the norm squared of the electric field components, the mode profiles were obtained at the resonant wavelengths (tabulated in Table 1). The mode profiles that correspond to the observed modes are shown below.

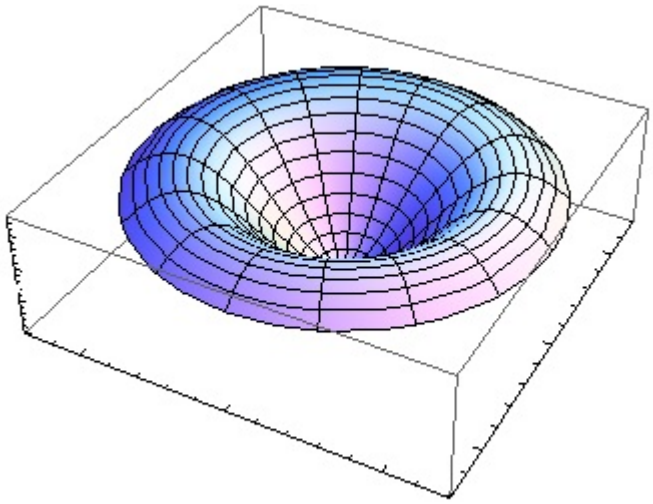

Figure S11: Guided TE_{01} mode

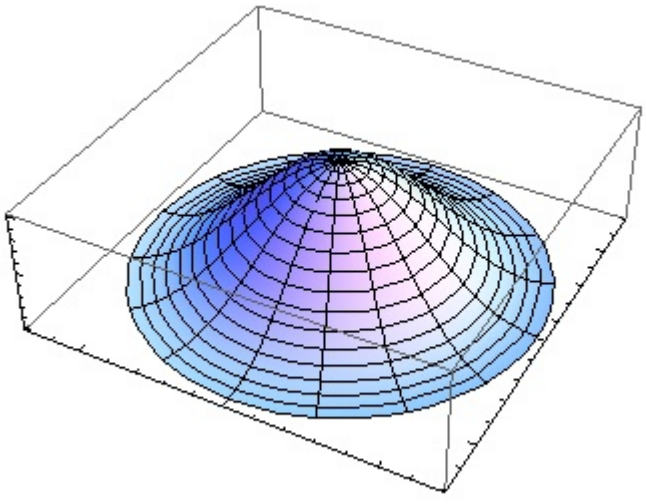

Figure S12: Guided TM_{01} mode

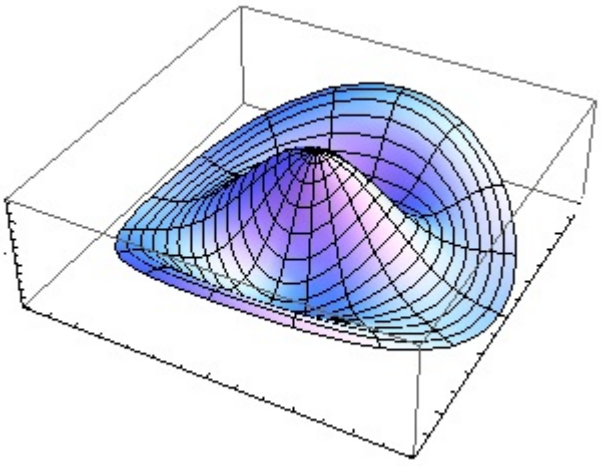

Figure S13: Leaky TE_{11} mode

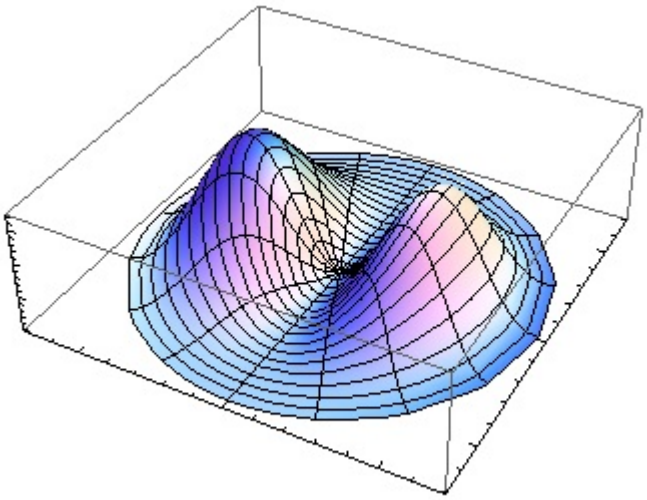

Figure S14: Leaky TM_{11} mode

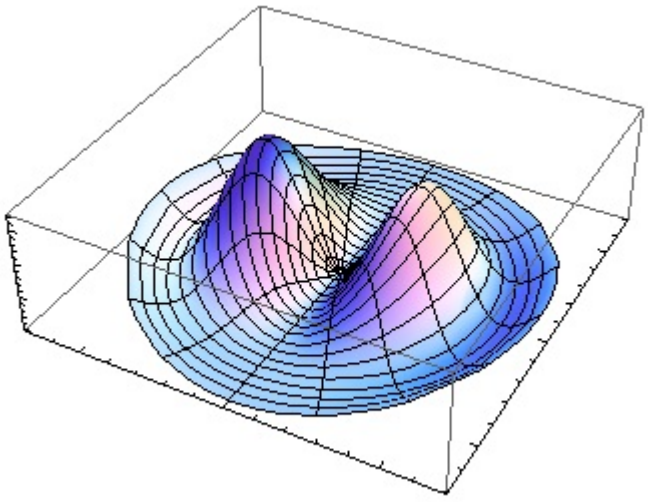

Figure S15: Leaky TM_{12} mode

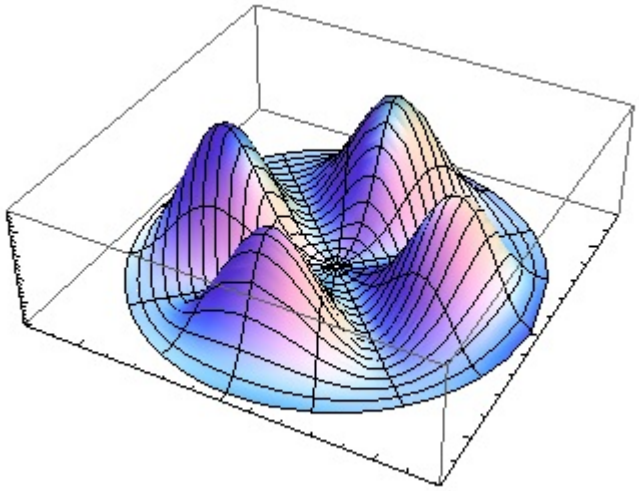

Figure S16: Leaky TM_{21} mode

References

1. Logeeswaran Vj, N. P. Kobayashi, M. S. Islam, W. Wu, P. Chaturvedi, N. X. Fang, S. Y. Wang, and R. S. Williams, *Nano letters*, 2009, **9**, 178–82.
2. A. Bard and L. Faulkner, *Electrochemical methods: fundamentals and applications*, Wiley, 1980.
3. S. W. Boettcher, J. M. Spurgeon, M. C. Putnam, E. L. Warren, D. B. Turner-Evans, M. D. Kelzenberg, J. R. Maiolo, H. a Atwater, and N. S. Lewis, *Science*, 2010, **327**, 185–7.
4. E. A. Santori, J. R. Maiolo III, M. J. Bierman, N. C. Strandwitz, M. D. Kelzenberg, B. S. Brunschwig, H. a. Atwater, and N. S. Lewis, *Energy & Environmental Science*, 2012, **5**, 6867.
5. K. E. Pomykal, A. M. Fajardo, and N. S. Lewis, *The Journal of Physical Chemistry*, 1996, **100**, 3652–3664.